Accurate Numerical Method of Calculating Frequency Distribution Functions in Solids. II. Extension to hcp Crystals*

L. J. RAUBENHEIMER† AND G. GILAT‡
Solid State Division, Oak Ridge National Laboratory, Oak Ridge, Tennessee
(Received 27 October 1966)

In a recent article by the same authors, an accurate and rapid method for calculating frequency distribution functions has been described. This method is here extended to include hexagonal close-packed crystals only, but it is shown that it can be used for crystals of any symmetry. This method is applied to beryllium, magnesium, and zinc, for which there exist satisfactory force models derived from experiments of inelastic coherent scattering of slow neutrons. These models have also been used to derive the phonon dispersion relations along nine high-symmetry directions, which are used to identify critical points observed in the frequency distribution functions. For each metal, there is at least one major critical point which could not be correlated to the high-symmetry branches. The phonon frequency distribution function $g(\nu)$ of beryllium indicates that it should be a favorable case for studying effects associated with heavy-impurity modes. The merits and also possible sources of error of this procedure are discussed. It is strongly recommended that the method be applied to calculations of electronic density of states.

I. INTRODUCTION

IN a recent article by the present authors[1] (hereafter to be referred to as GRI) an accurate and relatively rapid method for calculating phonon frequency distribution functions $g(\nu)$ in solids has been described. The so-called extrapolation method, an extension of an earlier version by Gilat and Dolling,[2] has been developed and applied in GRI to cubic crystals. In the present article, the method is extended to include hexagonal close-packed crystals in particular, but it will be deduced that it can be generalized to include crystals of any symmetry.

The extrapolation method, to describe it briefly, consists of solving the secular equation associated with the phonon dynamical matrix at a relatively small number of mesh points in the irreducible section of the first Brillouin zone (hereafter to be referred to as the "irreducible zone"), and then by means of linear extrapolation, extracting "all" the other solutions (i.e., phonon eigenfrequencies) from within small cubes, each centered at a mesh point. These cubes are so arranged as to fill the entire irreducible zone, and thus yield the complete frequency distribution function of the crystal. As a matter of principle, the detailed way in which the irreducible zone is filled is immaterial, as long as this is done properly, i.e., without overlaps or gaps. This means that the mesh of points chosen need not be uniform, and the shape of the volume surrounding each point does not have to be cubic either. Moreover, the statistical weight of each mesh point, which is usually associated with the point symmetry, now becomes obsolete. This can easily be realized by comparing the root-sampling method, which employs only a small number of points in the irreducible zone, to the present method which, in contrast, uses the entire volume of this zone. In the sampling method, only selected points are used to represent the entire irreducible zone. Some of these points are of higher symmetry, and are equally shared by two or more irreducible zones; hence they have to be given correspondingly lower weights. If the entire volume of this zone, rather than a finite number of points, is utilized, these weights become redundant. In GRI, however, it was still convenient to use weighting factors, to correct for over-filling of the irreducible zone. For the hcp crystals to be treated in this article, the irreducible zone is filled exactly by rectangular and triangular prisms, and hence no use is made of weighting factors. The mesh of points is relatively uniform, only for the sake of simplicity, but this is by no means obligatory. It is interesting, however, to point out that the problem of finding a uniform mesh of points in sampling methods can be intriguing for symmetries lower than cubic. This problem and that of weighting factors are avoided by using the extrapolation method, and this can be regarded as another advantage, in addition to the more important ones of high accuracy and rapidity.

The method is outlined in Sec. II in a fairly extensive manner, although some detailed analysis is included in Appendix A. In Sec. III we discuss the existing force models for three hcp metals, namely, beryllium, magnesium, and zinc. We also derive their dispersion curves along all nine high-symmetry directions in the first Brillouin zone. Section IV describes the actual computation of the distribution functions and possible correlation of the Van Hove critical points to the dispersion curves. In Sec. V we summarize the results of the computations and discuss merits and possible sources of error.

* Research sponsored by the U. S. Atomic Energy Commission under contract with the Union Carbide Corporation.
† Guest scientist from the South African Atomic Energy Board. Present address: South African Atomic Energy Board, Pretoria, South Africa.
‡ Present address: Department of Physics, Technion, Israel Institute of Technology, Haifa, Israel.
[1] G. Gilat and L. J. Raubenheimer, Phys. Rev. 144, 390 (1966) (to be referred to as GRI throughout this article). There is a mistake in Eq. (16) of this reference; the factor $2b^2$ of the first term should be replaced by b^2.
[2] G. Gilat and G. Dolling, Phys. Letters 8, 304 (1964).

II. THE METHOD

The general features of this method are adequately described[1] in GRI, so that only significant deviations from the treatment of the cubic system will be described here in more detail. Although our particular interest in this article is the application of the method to hexagonal crystals, it will be immediately observed from its very nature, that the same procedure can be applied in a more or less straightforward manner to any symmetry. In order to understand the changes necessary for adopting the method for noncubic crystals, a good starting point would be Eqs. (20) and (21) in GRI. These expressions, if properly interpreted, can readily be generalized to any symmetry. In Eq. (20) in GRI, i.e.,

$$g(\nu)=\sum_{j,\mathbf{q}_c} g(j,\mathbf{q}_c;\nu), \tag{1}$$

$g(\nu)$ is the final frequency distribution function which is obtained by summing $g(j,\mathbf{q}_c;\nu)$ over the mesh points $\mathbf{q}_c$ and over the set of eigenvalues of the dynamical matrix $\mathbf{D}(\mathbf{q}_c)$. The function $g(j,\mathbf{q}_c;\nu)$ is a partial frequency distribution function obtained by extrapolating the jth eigenvalue throughout a volume containing the point $\mathbf{q}_c$. Now, this volume does not have to be cubic, and, moreover, $\mathbf{q}_c$ need not be at its center (although for simplicity, this is mostly the case); what is required, is that these volumes will eventually fill the irreducible zone in an exhaustive manner. The explicit expression for $g(j,\mathbf{q}_c,\nu)$ is given by Eq. (21) of GRI, i.e.,

$$\begin{aligned} g(j,\mathbf{q}_c,\nu)d\nu &= CW_{\mathbf{q}_c}S(w)dw \quad \text{for} \quad \nu_{0j}-w_4|\operatorname{grad}\nu|_{\mathbf{q}_c} \\ &\qquad <\nu<\nu_{0j}+w_4|\operatorname{grad}\nu|_{\mathbf{q}_c} \\ &=0 \quad \text{elsewhere.} \end{aligned} \tag{2}$$

In this expression, C is an arbitrary constant[3]; $S(w)$ is the cross-section area of a prism at a distance w from $\mathbf{q}_c$ measured along the direction of $(\operatorname{grad}_q\nu_j)_{\mathbf{q}=\mathbf{q}_c}$; $W_{\mathbf{q}_c}$ is a weighting factor, which becomes redundant, if the irreducible zone is filled exactly; w_4 is defined in GRI. In the cubic case, however, there were some mesh points located on the surface of the irreducible zone, and it was much more convenient to extrapolate $\nu_{0j}(\mathbf{q}_c)$ at these points throughout small cubes belonging partly to neighboring zones. In other words, the irreducible zone was over-filled to some extent, but this was readily compensated for by using $W_{\mathbf{q}_c}$ obtained from symmetry properties of these points. For the hcp lattice, however, the irreducible zone is filled exactly, and hence no use is made of weighting factors.

In order to find the best way of filling the irreducible zone for any given symmetry, each individual case has to be examined separately. We now treat the hcp case. The first Brillouin zone of an hcp crystal is shown in Fig. 1 together with the location of the high-symmetry

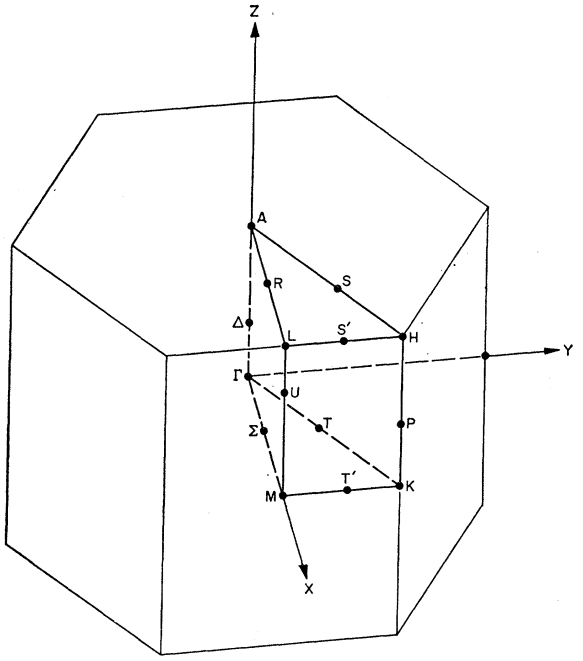

FIG. 1. First Brillouin zone for a hcp lattice. The irreducible zone is indicated in particular.

points and directions as specified by Koster.[4] We adopt the same Cartesian frame as DeWames, Wolfram, and Lehman,[5] which is rotated by 90° from that of Koster.[4] The irreducible zone, which is 1/24 of the full first Brillouin zone, is included within the following five planes: ΓMK, ALH, $LMKH$, ΓMLA, and ΓKHA. In Fig. 2 this wedge-shaped figure is shown on an enlarged scale; the way in which this shape is filled by rectangular and triangular prisms is schematically demonstrated. Each mesh point $\mathbf{q}_c$ is located at the center of a rectangular prism, except for those on the surface ΓKHA. The latter belong to triangular prisms which are similar in shape to the irreducible zone itself; each such mesh point is situated at the center of the face which coincides with the plane ΓKHA.

Once the way of filling the irreducible zone is decided, all that remains is to work out the expressions for the cross-section areas $S(w)$ suitable for both prisms. In the case of the rectangular prism the generalization from the cubic case discussed[1] in GRI [Eqs. (12) through (18)] is very simple. Let us denote the lengths of the three sides of this prism by $2a_\alpha(\alpha=x, y, z)$, and then define λ_α by

$$\lambda_\alpha=l_\alpha a_\alpha, \tag{3}$$

where l_α are the direction cosines of the gradient of ν_{0j} at $\mathbf{q}_c$. The λ_α can be ordered as follows:

$$\lambda_1\geqslant\lambda_2\geqslant\lambda_3\geqslant 0. \tag{4}$$

[3] The exact value of C is associated with the total number of normal modes in a crystal of a given physical volume.

[4] G. F. Koster, in *Solid State Physics*, edited by F. Seitz and D. Turnbull (Academic Press Inc., New York, 1957), Vol. 5, p. 173.

[5] R. E. DeWames, T. Wolfram, and G. W. Lehman, Phys. Rev. **138**, A717 (1965).

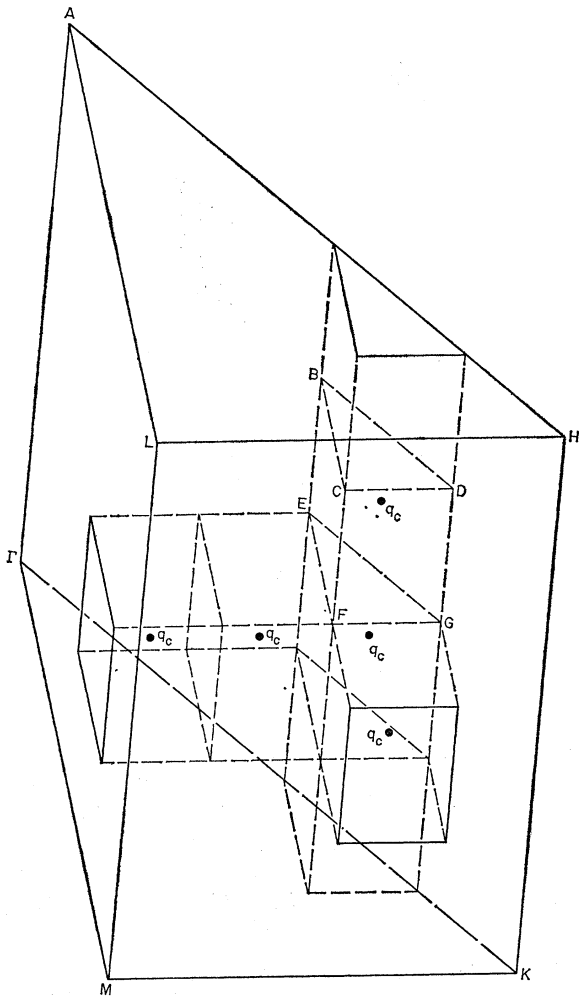

FIG. 2. A simple way to fill the irreducible zone by rectangular and triangular prisms. The mesh points $\mathbf{q}_c$ are at the center of each of the rectangular prism. For the triangular prisms each $\mathbf{q}_c$ is at the center of that surface which lies in the plane ΓKHA.

The equation equivalent to Eq. (13) in GRI is

$$\begin{aligned} w_1&=|\lambda_1-\lambda_2-\lambda_3|\,,\\ w_2&=\lambda_1-\lambda_2+\lambda_3\,,\\ w_3&=\lambda_1+\lambda_2-\lambda_3\,, \end{aligned} \tag{5}$$

and

$$w_4=\lambda_1+\lambda_2+\lambda_3\,,$$

where w_i are the distances of the four corners of the rectangular prism from a plane having the same direction cosines and passing through $\mathbf{q}_c$. The shapes that the cross-section area $S(w)$ can take on are similar to those of the cube. Again, as in GRI, for the first range $(0,w_1)$, there are two possibilities depending on the sign of $(\lambda_1-\lambda_2-\lambda_3)$. If the sign is positive, we have a parallelogram of area

$$S(w)=V/2\lambda_1 \quad \text{for} \quad \lambda_1\geq\lambda_2+\lambda_3, \quad (0\leq w\leq w_1), \tag{6}$$

where V is the volume of the rectangular prism:

$$V=8a_1a_2a_3. \tag{7}$$

If $(\lambda_1-\lambda_2-\lambda_3)$ is negative, the cross section is hexagonal of area

$$\begin{aligned} S(w)=(V/8\lambda_1\lambda_2\lambda_3)[&2(\lambda_1\lambda_2+\lambda_2\lambda_3+\lambda_3\lambda_1)\\ &-(w^2+\lambda_1^2+\lambda_2^2+\lambda_3^2)] \end{aligned}$$

$$\text{for} \quad \lambda_1\leq\lambda_2+\lambda_3 \quad \text{and} \quad 0\leq w\leq w_1. \tag{8}$$

In the second range (w_1,w_2), we have a pentagon of cross section

$$\begin{aligned} S(w)=(V/8\lambda_1\lambda_2\lambda_3)[&3\lambda_2\lambda_3+\lambda_1\lambda_2+\lambda_3\lambda_1\\ &-w(-\lambda_1+\lambda_2+\lambda_3)-\tfrac{1}{2}(w^2+\lambda_1^2+\lambda_2^2+\lambda_3^2)]. \end{aligned} \tag{9}$$

For the third range (w_2,w_3), the shape is a quadrangle of area

$$S(w)=(V/4\lambda_1\lambda_2\lambda_3)[\lambda_3(\lambda_1+\lambda_2)-w\lambda_3]. \tag{10}$$

Finally for (w_3,w_4), the shape is triangular, with

$$S(w)=(V/16\lambda_1\lambda_2\lambda_3)(\lambda_1+\lambda_2+\lambda_3-w)^2. \tag{11}$$

All these expressions should be even functions of w, so that for $w<0$, w has to be replaced by $|w|$. The typical behavior of these functions is shown in GRI, Fig. 1.

Slightly more complicated is the case of the triangular prisms by which we fill the irreducible zone along the surface ΓKHA. For instance, the cross-section area is no longer an even function of w. The number of different possible ways in which a plane can sweep across the prism is appreciably higher. We refer the reader to a detailed treatment of this case in Appendix A, but a few things in this connection might be mentioned here. A very helpful and general geometrical property of the cross-section area $S(w)$ can be employed in more complicated cases. This property is explained in the following discussion: Let a plane P sweep across a simple polyhedron, so that it is always perpendicular to a given direction. If w is the distance of P from any given point, and $S(w)$ is the cross-section area of the polyhedron with respect to P, then $S(w)$ and dS/dw are both continuous functions of w whenever the plane passes through a corner point of the polyhedron, as long as P is not parallel to any of the polyhedron edges or surfaces.[6] This fact was observed in GRI for the cubic case, and has been applied here to the triangular prism (see Appendix A). Another helpful feature is the symmetry property of the mesh points $\mathbf{q}_c$ chosen to lie on the surface ΓKHA of the irreducible zone. This surface, being a mirror plane, implies that the gradient of $\nu_j(\mathbf{q}_c)$

[6] It is interesting to note that if this plane is parallel to one or more edges, then whenever it sweeps across such an edge, dS/dw suffers a discontinuity. Likewise, if the plane is parallel to one or more surfaces, $S(w)$ itself is discontinuous when the plane sweeps across such a surface. On the other hand, if the plane happens to sweep simultaneously through more than one corner point, which do not lie on the same edge or surface, no such discontinuity is encountered.

must lie in this surface, which considerably simplifies treatment of the triangular prism.

Having obtained $S(w)$ for the rectangular and the triangular prism (Appendix A), $g(\nu)$ is obtainable in a straightforward manner, from Eq. (2), in which W_{q_c} is unity, and Eq. (1).

III. DISPERSION RELATIONS AND FORCE MODELS

In the case of cubic lattices without a basis, it is possible, in principle, to measure $g(\nu)$ by incoherent inelastic scattering of slow neutrons—a method which cannot be employed for crystals possessing a nonprimitive translation.[7] In most cases, however, the only way to obtain $g(\nu)$ is by calculation. In order to calculate $g(\nu)$ of a crystal, it is necessary to have some force model which adequately describes the phonon dispersion relations of the crystal. So far, the best source for this information has been the measurement of dispersion curves by inelastic coherent scattering of slow neutrons.

In this section we present the dispersion relations of phonons along nine high-symmetry directions: Δ, Σ, T, T', R, S, S', P, and U (Fig. 1). These dispersion relations were derived from force models for three hcp crystals, namely Be, Mg, and Zn, for which there exist relatively accurate experimental data. Dispersion relations in Be were measured by Schmunk[8] *et al.*, along the $\Delta(0001)$ and $\Sigma(01\bar{1}0)$ directions (Fig. 1), and more recently by Schmunk[9] along some of the branches of the T direction $(11\bar{2}0)$. In these experiments the time-of-flight technique was employed. In Mg, the phonon spectrum was measured along the Δ and Σ directions by Iyengar *et al.*[10] using the triple-axis spectrometer, and by Squires[11] along the T, T', and Σ directions using the chopper technique. In Zn it was observed for the Δ and Σ directions by Borgonovi *et al.*,[12] who used a three-axis spectrometer. Unfortunately, the measured branches, together with the elastic constants, allow the determination of only a limited number of independent force constants. DeWames *et al.*[5] made use of the data of Be[8] and Zn[12] and derived a Born–von Kármán force model, the so-called "modified axially symmetric model" (MAS), which fits the experimental data reasonably well. The main feature of this model is that it describes interactions between neighbors by at most three independent force constants, rather than the possible six force constants allowed by the most general force model. This permits more flexibility in fitting the MAS model to the phonon dispersion curves as well as to the elastic constants, compared to the restricted axially symmetric model (AS) which allows only two such force constants per neighbor. On the other hand, the MAS model enabled DeWames *et al.*[5] to extend the range of interaction to include as many as six nearest neighbors. This is obviously in accord with present-day theories of phonon dispersion relations in metals which indicate long-range interactions in metals. Iyengar *et al.*[10] were able to fit their data to a four-neighbor tensor-force model (TF), which includes only eleven force constants out of a possible fourteen. Since eleven is exactly the number of force constants required by the four-neighbor MAS model, it is possible to establish a one-to-one correspondence between the TF and MAS models for this special case. In Appendix B we give the relations between these two models. The MAS model is used throughout this article. The appropriate expressions for the dynamical matrix elements are given by DeWames *et al.*[5] in their Appendix A. This Hermitian (6×6) dynamical matrix $\mathbf{D}(\mathbf{q})$ can be transformed into a real symmetric matrix $\mathbf{M}(\mathbf{q})$ by applying the unitary transformation:

$$\mathbf{U}=\frac{1}{\sqrt{2}}\begin{bmatrix} I & iI \\ iI & I \end{bmatrix}, \tag{12}$$

where I is a (3×3) unit matrix, so that:

$$\mathbf{M}(\mathbf{q})=\mathbf{U}^{\dagger}\mathbf{D}(\mathbf{q})\mathbf{U}=\frac{1}{2}\begin{bmatrix} \mathbf{D}^{11}-\mathrm{Im}\mathbf{D}^{12} & \mathrm{Re}\mathbf{D}^{12} \\ \mathrm{Re}\mathbf{D}^{12} & \mathbf{D}^{11}+\mathrm{Im}\mathbf{D}^{12} \end{bmatrix}, \tag{13}$$

where $\mathbf{D}^{11}$ and $\mathbf{D}^{12}$ are (3×3) matrices defined by

$$\mathbf{D}(\mathbf{q})=\begin{bmatrix} \mathbf{D}^{11}(\mathbf{q}) & \mathbf{D}^{12}(\mathbf{q}) \\ \mathbf{D}^{12}(\mathbf{q})^{*} & \mathbf{D}^{11}(\mathbf{q}) \end{bmatrix}. \tag{14}$$

Before proceeding to derive the phonon dispersion curves for each material, it should be mentioned that the problem of deriving a Born–von Kármán force model for hcp lattices is far more complicated than it is for cubic crystals. This is partly due to mathematical difficulties associated with the lower symmetry, but it is mainly due to the presence of two sublattices in hcp crystals. The two sublattices make it impossible to express interatomic force constants as linear combinations of interplanar force constants, the latter being the natural Fourier components which describe the different modes of vibration along high-symmetry directions. Because of this difficulty, it is expected that Born–von Kármán force models will not describe phonon dispersion relations in hcp crystals to as high accuracy as in cubic metals. Moreover, the existing experimental data for hcp metals are rather meager, in the sense that only relatively few high-symmetry directions out of all possible ones have actually been examined. This limits

[7] G. Placzek and L. Van Hove, Phys. Rev. **93**, 1207 (1954).
[8] R. E. Schmunk, R. M. Brugger, P. D. Randolph, and K. A. Strong, Phys. Rev. **128**, 562 (1962).
[9] R. E. Schmunk, Phys. Rev. **149**, 450 (1966). We are indebted to the author for sending us a copy of his paper prior to publication.
[10] P. K. Iyengar, G. Venkataraman, P. R. Vijayaraghavan, and A. P. Roy, in *Inelastic Scattering of Neutrons in Solids and Liquids*, (International Atomic Energy Agency, Vienna, 1965), Vol. I, p. 153.
[11] G. L. Squires, Proc. Phys. Soc. (London) **88**, 919 (1966).
[12] G. Borgonovi, G. Caglioti, and J. J. Antal, Phys. Rev. **132**, 683 (1963).

the number of independent parameters for a given set of neighbors that can be obtained from the data. In addition, there exists the well-known phenomenon of long-range interactions in metals, which may require many more neighbors to fit adequately the phonon dispersion curves in order to obtain a reliable interpolation formula for the purpose of calculating $g(\nu)$. In view of all these comments, it is not surprising that the models calculated by DeWames *et al.*[5] for Be [8] and Zn [12] and by Iyengar *et al.*[10] for Mg are only barely adequate to describe the measured phonon dispersion curves. Furthermore, they might not be adequate at all for the purpose of calculating dispersion relations along other directions, and hence for calculating $g(\nu)$. Nevertheless, in the absence of better models, we use the given ones to calculate the dispersion curves for all high-symmetry directions, because it is desirable to find correlations between Van Hove critical points in $g(\nu)$ and the behavior of the dispersion relations. In presenting the dispersion curves along all high-symmetry directions, namely Σ, T, T', R, S, S', Δ, P, and U (Fig. 1), we classify them according to the allowable irreducible representations of the invariant subgroup of symmetry operations, which is associated with each high-symmetry direction and point. We use the notation given by Iyengar *et al.*,[10] who obtained the irreducible representations for some of these points and directions. Similar notation is used for the rest of the points and directions. The classification of modes by allowable irreducible representation is described in Appendix C, together with some compatibility relations, which join points to curves in a consistent manner. If more than one mode belongs to the same representation, they are distinguished by the label A (acoustic) for the lowest

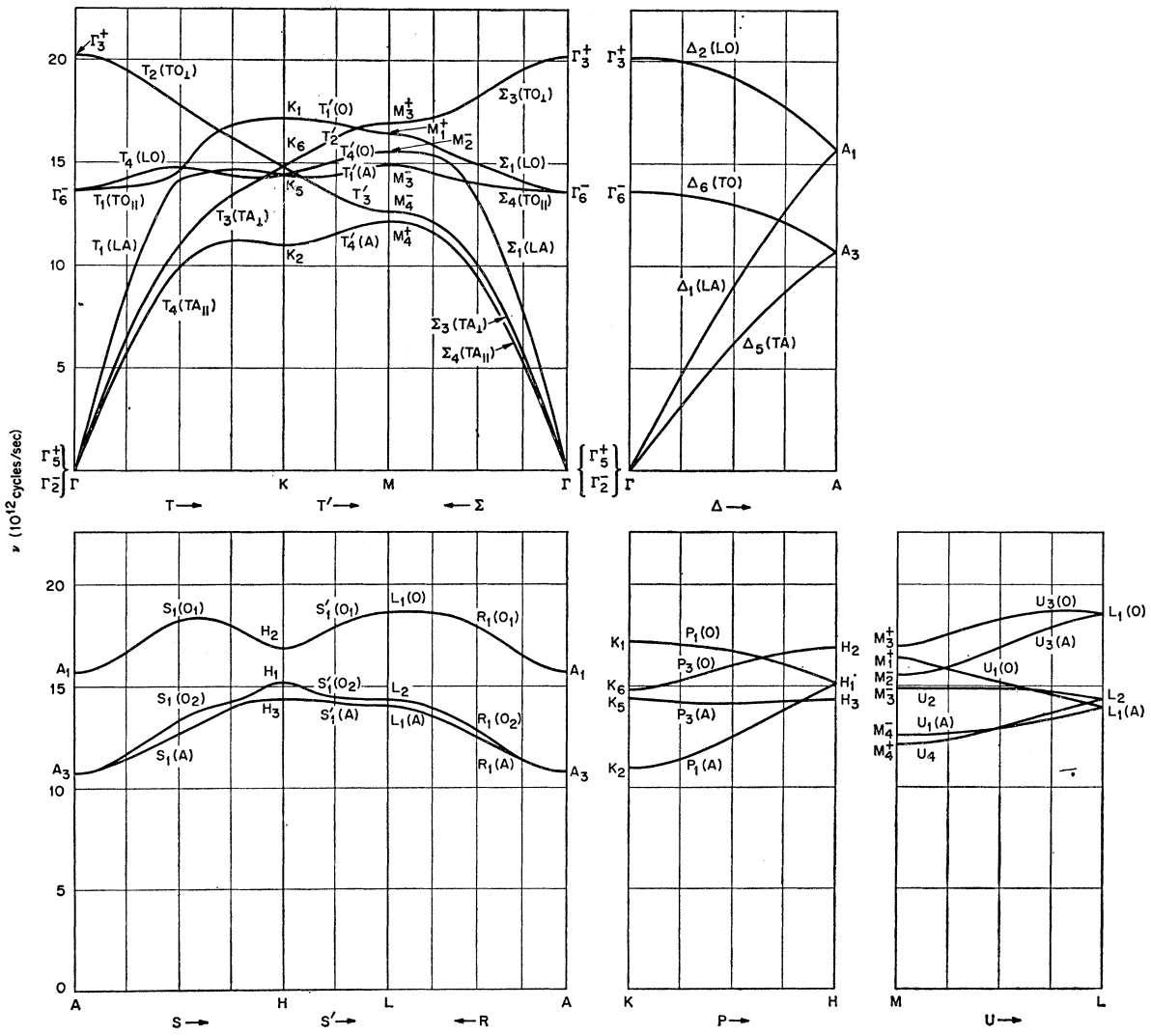

FIG. 3. Phonon dispersion relations for beryllium, calculated from the MAS model of DeWames, Wolfram, and Lehman (Ref. 5).

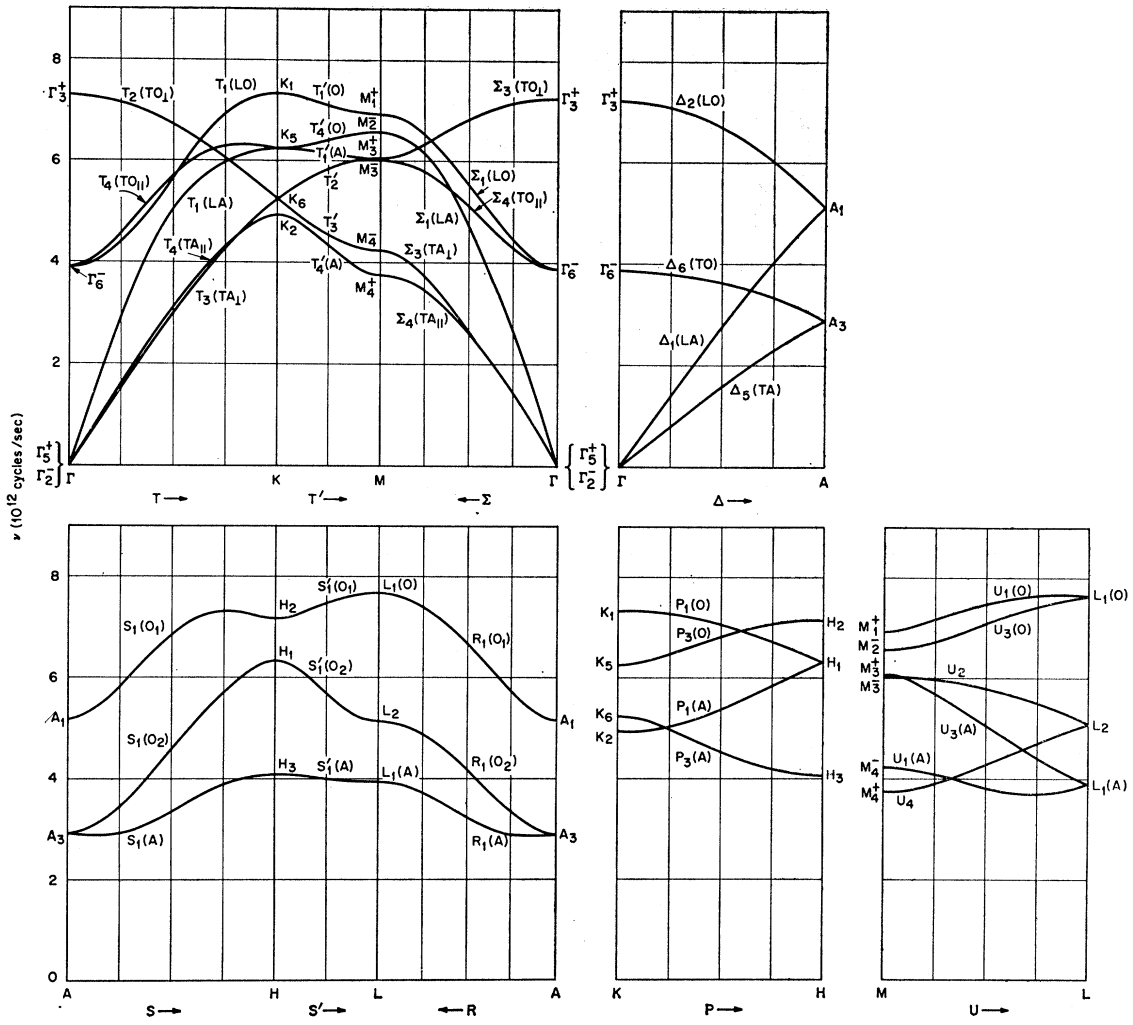

FIG. 4. Phonon dispersion relations for magnesium, calculated from a TF model by Iyengar *et al.* (Ref. 10).

mode and O_1, O_2, etc. (optic) for the higher modes, starting from O_1 for the highest. We now describe the three individual cases.

Beryllium

The calculated phonon dispersion curves are shown in Fig. 3. The force model used to obtain these curves is a six-neighbor MAS model, given by DeWames *et al.*[5] The scale for the **q** vector in all the basal directions (Fig. 1) is the same, but a different scale, which does not take into account the c/a ratio, has been used for the vertical directions Δ, P, and U. It is interesting to note that symmetry requires six different bands for the basal directions T, T', and Σ, whereas only three, each doubly degenerate, exist for the basal directions S, S', and R. This simplification can be misleading, since the polarizations for the latter are considerably more complicated. The vertical directions Δ, P, and U consist of three, four, and six bands, respectively. More details about symmetry requirements and degeneracies can be found in Appendix C.

Magnesium

The phonon dispersion curves are shown in Fig. 4. The force model used for the calculation of these curves is a four-neighbor TF model given by Iyengar *et al.*,[10,13] which has been transformed to the MAS model using the relations of Appendix B. The frequencies of M_3^+ and M_3^- are very close, M_3^+ being slightly higher. It is interesting to note that the highest frequency for the spectrum according to this model occurs along the branch $U_1(0)$, which has not been studied experimentally.

[13] P. K. Iyengar, G. Venkataraman, P. R. Vijayaraghavan, and A. P. Roy, Lattice Dynamics, in *Proceedings of the International Conference on Lattice Dynamics Copenhagen, 1963*, edited by R. F. Wallis (Pergamon Press, Inc., New York, 1965), p. 223.

Zinc

The dispersion curves are shown in Fig. 5. The model used for the calculation is a six-neighbor MAS model given by DeWames *et al.*[5] Comparison of Zn with Be and Mg shows that Zn is a considerably more anisotropic material. This fact is displayed by the appreciable difference between the two acoustic transverse branches $\Sigma_3(\mathrm{TA}_\perp)$ and $\Sigma_4(\mathrm{TA}_{\parallel})$ along Σ, and $T_2(TA_\perp)$ and $T_1(TA_{\parallel})$ along T. In both Be and Mg those branches are almost degenerate, whereas in Zn an appreciable difference is observed. Another interesting feature is the considerably higher frequencies at M_2^- and M_1^+ compared to the optic ends at $\mathbf{q}=0$ (Γ_6^- and Γ_3^+). The almost flat bands along the P and the U directions are also of significance. An interesting phenomenon occurs along the S direction very close to the point H and again along the R direction. The bands along S and R all belong to the same irreducible representations, respectively, and as such cannot intersect.[14] While a careful analysis has shown that the bands along S are actually split by a very small gap (in fact too small to be observed in Fig. 5), the degeneracy along R does still exist. Nevertheless, this accidental degeneracy is spurious and model-dependent, and it arises because the MAS model imposes some extra restrictions on the force constants, which are not required by symmetry. For instance, under these restrictions, the imaginary part of the dynamical matrix element $D_{12}{}^{11}(\mathbf{q})$ is zero,

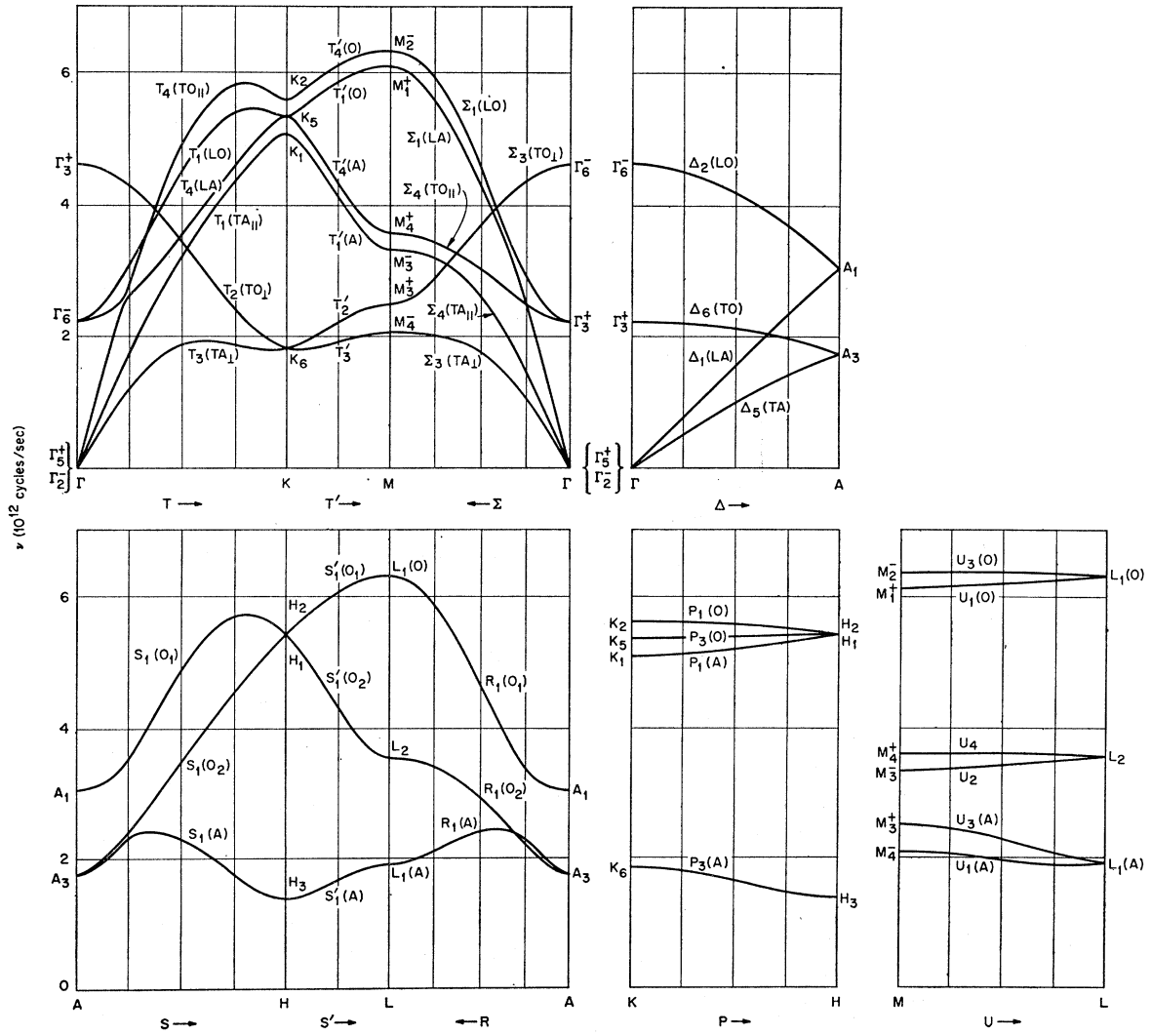

FIG. 5. Phonon dispersion relations for zinc, calculated from the MAS model of DeWames *et al.*, (Ref. 5). See text concerning accidental degeneracies.

[14] J. von Neumann and E. P. Wigner, Z. Physik **30**, 467 (1929); see also a paper by C. Herring [Phys. Rev. **52**, 365 (1937)] on accidental degeneracies.

and so is the real part of $D_{23}^{12}(\mathbf{q})$; as a matter of fact, it is possible to remove this degeneracy by "violating" these MAS restrictions.

IV. COMPUTATION OF $g(\nu)$

The method of calculating $g(\nu)$ outlined[1] in GRI and in Sec. II of the present article (see also Appendix A) has been applied to the three hcp lattices discussed in Sec. III. The irreducible zone (1/24 of the first Brillouin zone) is divided into a mesh of points, none of which lies on any of the high-symmetry points or directions. This is in order to avoid degeneracies required by symmetry. In GRI we referred to such a mesh[2] as a "shifted" mesh. More technical details about the construction of the mesh can be found in Appendix D. A few meshes with different numbers of points have been tried for each lattice in order to detect any systematic changes due to the mesh fineness. Apart from minor changes, which mainly tend to smooth the curves of $g(\nu)$ as the mesh becomes finer, no such systematic changes have been observed. The number of mesh points was around 3000 in the cases described and the computing time was of the order of 30 min. The computer program used was very similar in its essentials to the one[15] described in GRI. All the curves of $g(\nu)$ to be presented are the actual unsmoothed computer plots. All the computations described in this section were performed on the CDC-1604 A computer at the Oak Ridge National Laboratory.

Only in the case of Be do we proceed beyond the computation of $g(\nu)$ to draw thermodynamic conclusions. The reason for this is that unless anharmonic effects are small, one cannot use $g(\nu)$ derived from inelastic scattering of neutrons to calculate the Debye temperature Θ^c appropriate to the specific heat.[16] We have no reason to believe that this is the case for Mg and Zn, since the Θ^c are of the order of 300°K, the temperature at which the data were taken. For Be the case is different, since its Θ^c is considerably larger than 300°K. We are also hesitant to draw too far-reaching conclusions because of the obvious discrepancies between the models and the experimental results, which we consider quite significant. An attempt to correlate the expected critical points from the dispersion curves to those observed in the different distribution functions is summarized in Table I for all three crystals. In the first column we give the group-theoretical assignment of branches or points of the dispersion curves. For each element we give the corresponding frequency and the type of criticalness, where M represents maximum, m stands for minimum, and I for any other type of zero gradient, such as saddle point. We also give the strength of each point as it appears on the curves of $g(\nu)$. We classify the strength in a somewhat subjective way: s represents a "strong" critical point, w a "weak" one, and a stands for "absent" points, i.e., for expected critical points that do not appear on $g(\nu)$. Also listed in Table I are the conspicuous critical points that are not predicted by the dispersion curves, and hence are associated with off-symmetry branches. Individual cases of $g(\nu)$ are discussed in the following sections.

Beryllium

The number of mesh points chosen for the computation of the phonon frequency distribution function $g(\nu)$ was 2520. The histogram of $g(\nu)d\nu$ is sorted into about 1000 channels of $d\nu=0.02\times10^{12}$ cps, and is shown in Fig. 6. A very striking feature of this spectrum is the large frequency range of relatively low density of phonon states. This makes Be a very suitable host for heavy impurities in order to study their resonance-mode frequencies. Unfortunately, the relatively complicated hcp structure makes such an investigation a fairly difficult one. This low density is presumably also the reason why low-temperature heat-capacity data for Be are so sensitive to the purity of the crystal.[17–19]

Critical points expected from the dispersion curves are indicated in Fig. 6. There are two critical points at 17.07 and 18.53 (in units of 10^{12} cps) which cannot be predicted from the dispersion relations. A full list of all the critical points is given in Table I.

Since Θ^c for Be is considerably higher than 300°K, the temperature at which the data were taken, anharmonic effects should not be very significant. We therefore calculated Θ^c as a function of temperature, and obtained $\Theta^c(0°)=1437\pm3$°K and $\Theta^c(T\rightarrow\infty)$

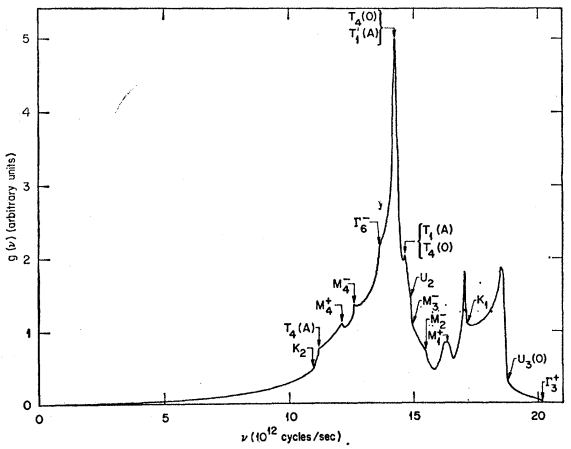

FIG. 6. Unsmoothed computer plot of phonon frequency distribution function for beryllium. Indicated critical points are predicted from dispersion curves in Fig. 3.

[15] L. J. Raubenheimer and G. Gilat, Oak Ridge National Laboratory Report No. ORNL TM-1425 1966 (unpublished).

[16] T. H. K. Barron, in *Proceedings of the International Conference on Lattice Dynamics, Copenhagen, 1963*, edited by R. F. Wallis (Pergamon Press, Inc., New York, 1965), p. 247.

[17] R. W. Hill and P. L. Smith, Phil. Mag. **44**, 636 (1953).

[18] M. E. Gmelin, Compt. Rend. **259**, 3459 (1964).

[19] G. Ahlers, Phys. Rev. **145**, 419 (1966).

TABLE I. List of the critical points in Be, Mg, and Zn. In the first column we identify the high-symmetry branch or point from which the critical point is predicted. For each element we list the frequency at the critical point, when its topological nature (where M is maximum, m is minimum, and I encompasses all the other cases for which there exist a zero gradient, such as a saddle point). In the last column for each case we specify the strength of the critical points as they show up in $g(\nu)$ (s stands for "strong," w for "weak," and a for "absent"). At the bottom of the table we give a few very pronounced critical points which cannot be predicted from the high-symmetry dispersion curves.

Assignment	Beryllium $\nu(10^{12}$ cps)	Beryllium Topological nature	Beryllium Strength	Magnesium $\nu(10^{12}$ cps)	Magnesium Topological nature	Magnesium Strength	Zinc $\nu(10^{12}$ cps)	Zinc Topological nature	Zinc Strength
Γ_3^+	20.20	M	s	7.28	M	w	4.61	M	w
Γ_6^-	13.64	M	s	3.90	M	s	2.23	M	s
$T_1(0)$							5.54	M	s
$T_1(A)$	14.67	M	s						
T_3							1.79	m	s
							1.93	M	s
$T_4(0)$	14.66	M	s	6.34	M	s	5.83	M	s
	14.28	m	s						
$T_4(A)$	11.20	M	s						
K_1	17.14	M	$w(a)$	7.35	M	a	5.07	M	w
K_2	11.01	m	w	4.95	M	$w(a)$	5.58	M	a
$T_1'(A)$	14.27	m	s	6.265	M	s			
$T_4'(O)$					m				
T_3'							1.80	m	s
M_1^+	16.42	I	w	6.96	I	s	6.10	M	s
M_2^-	15.53	I	s	6.59	I	s	6.33	M	s
M_3^+	16.95	I	a	6.08	I	s	2.49	I	s
M_3^-	14.91	M	$w(a)$	6.07	M	w	3.32	I	s
M_4^+	12.14	I	s	3.77	I	s	3.58	I	s
M_4^-	12.62	I	s	4.25	I	s	2.04	M	a
$S_1(O_1)$	18.35	M	a	7.31	M	w	5.70	M	a
$S_1(A)$				2.89	m	a			
H_2	16.89	m	a	7.17	I	w	5.39	m	a
H_3	15.14	M	a	4.08	I	s	1.37	m	s
$R_1(O)$	18.63	M	a						
$R_1(A)$				2.89	m	a	2.44	M	a
$P_3(A)$	14.17	m	a						
$U_1(O)$				7.71	M	s			
$U_1(A)$				3.73	m	w	1.86	m	a
U_2	14.93	M	$w(a)$						
$U_3(O)$	18.74	M	$w(a)$				6.33	M	s
U_4							3.58	M	s
Not predicted	17.07		s	7.23		s	4.04		s
	18.53		s						

$=904°$K. The error indicates uncertainty originating only from the computation and is not to be understood as an experimental error. $\Theta^c(T)$ is a monotonically decreasing function and has no minimum. The range over which $\Theta^c(T)$ varies is unusually large, and can be explained by the peculiar shape of $g(\nu)$. It is interesting to compare the above result of $\Theta^c(0°)$ to earlier measurements and calculations. As was indicated earlier, $\Theta^c(0°)$ is very sensitive to the purity of the crystal. Hill and Smith[17] measured a value of $\Theta^c(0°)=1160°$K for a sample 99.5% pure. Gmelin[18] obtained 1390°K for a sample of Be containing less than 100 ppm impurities. Ahlers[19] used a still more pure specimen and obtained $1481\pm16°$K. The value calculated by Alers and Neighbours[20] from the 0°K elastic constants measured by Smith and Arbogast[20] is $\Theta^c(0°)=1462°$K. DeWames *et al.*[19,21] calculated from their MAS model a few values of $\Theta^c(T)$ which lead to a value of 1470°K at 0°K. The last value is a little surprising when compared to our value of 1437°K, since they are both derived from the same model and thus should be identical. We believe that the value of 1437°K is probably correct, because of the following reason. The values of the elastic constants predicted[5] by the MAS model are somewhat smaller than the values measured at 0°K. This is especially true for c_{44} and $\frac{1}{2}(c_{11}-c_{12})$, which dominate the Debye end of $g(\nu)$. It is therefore inconceivable that the MAS model would predict a value for $\Theta^c(0°\text{K})$ higher than 1462°K. A possible reason for this discrepancy could be that DeWames *et al.* used the ordinary root-sampling method, which leads to a statistically inadequate $g(\nu)$.

[20] J. F. Smith and C. L. Arbogast, J. Appl. Phys. **31**, 99 (1960).
[21] We obtained the value of $\Theta^c(0°)=1470°$K by extrapolating to 0°K in Fig. 2 of Ref. 19.

Magnesium

The $g(\nu)$ for magnesium is shown in Fig. 7. The number of mesh points was 3588 and the histogram was sorted into about 1500 intervals of width of 0.005×10^{12} cps. The critical points that can be predicted from the dispersion curves of Mg (Fig. 4) are indicated in Fig. 7. A full list of the critical points is given in Table I. A strong critical point that is not predicted by the high-symmetry branches appears at $\nu=7.23\times10^{12}$ cps. No

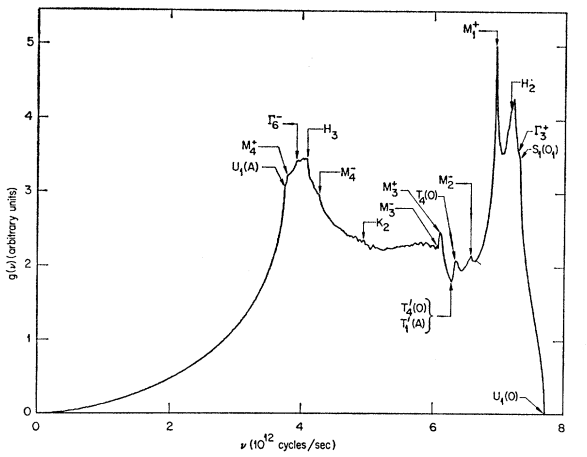

FIG. 7. Unsmoothed computer plot of phonon frequency distribution function for magnesium. Indicated critical points are predicted from dispersion curves in Fig. 4.

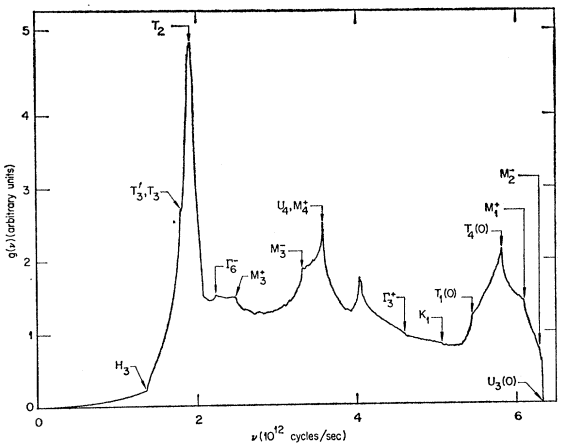

FIG. 8. Unsmoothed computer plot of phonon frequency distribution function for zinc. Indicated critical points are predicted from dispersion curves in Fig. 5.

attempt has been made to calculate Θ^c as a function of temperature, because anharmonic effects are bound to be appreciable at room temperature.

Zinc

The $g(\nu)$ for zinc is shown in Fig. 8. The number of mesh points utilized for this computation was 3600, and the histogram of $g(\nu)$ was sorted into about 2500 frequency intervals of $d\nu=0.0025\times10^{12}$ cps. The critical points predicted from the dispersion curves are indicated in Fig. 8, and a complete list is given in Table I. There is a strong critical point at $\nu=4.04\times10^{12}$ cps, which cannot be predicted from the high-symmetry branches. Another critical point seems to exist at $\nu=1.90\times10^{12}$ cps, very near to the highest peak in $g(\nu)$. It is interesting to note that this frequency is equal to that of the point $L_1(A)$ on the dispersion curves (Fig. 5). Symmetry does not require[22] a vanishing frequency gradient at point L (Fig. 1), and hence we do not expect a critical point associated with L. However, from observation of the dispersion relations along $U_1(A)$ and $U_3(A)$ very near $L_1(A)$, one can see that the z component of the gradients of the frequencies should be small.[22] In the vicinity of L, along any off-symmetry direction, the degeneracy at L has to be lifted. This implies small values for the components of the frequency gradient over some region around L, which might give rise to a critical point.[23] The same situation occurs for $L_1(0)$ at $\nu=6.28\times10^{12}$ cps, but if this caused a critical point, it would be a very minor one.

A striking feature of the phonon density of states $g(\nu)$ for Zn is its very small Debye range of frequencies. There is a strongly pronounced critical point associated with point H_3 at $\nu=1.37\times10^{12}$ cps, beyond which the shape of $g(\nu)$ assumes considerable structure. This structure would cause a strong temperature dependence of Θ^c, which can be demonstrated by the following calculated values: $\Theta^c(0°)=297°\text{K}$, $\Theta^c(\infty)=241°\text{K}$, with a deep minimum of $\Theta^c(20°\text{K})=199°\text{K}$. Because of anharmonic effects these values should not be taken seriously.

V. CONCLUSIONS

This is the first attempt to apply the extrapolation technique to any system other than cubic. For cubic systems the advantage in using the present method lies mainly in obtaining much higher resolution and accuracy in $g(\nu)$ together with a very substantial saving in computing time. For the hcp system the advantage is even more pronounced, because it is the first method that permits $g(\nu)$ to be obtained with high resolution and accuracy within a reasonable computing time. Moreover, the method can be extended in a perfectly straightforward manner to any lattice symmetry, but this might be a tedious task for lower symmetries. In claiming that this method is one of high accuracy and resolution, we mean that it is capable of producing fine features associated with any particular model. In other words, no information is lost via the use of this method and it would be capable of producing accurate predictions of physical properties if the model used were adequate. Unfortunately, most force models are still inadequate, and we would like to emphasize here the

[22] As a matter of fact, symmetry requires $\partial\nu/\partial q_x=\partial\nu/\partial q_y=0$ at L, but there are no restrictions on $\partial\nu/\partial q_z$.

[23] In this connection it is interesting to mention the mild critical point observed at $\nu=2.86\times10^{12}$ cps in Na (see GRI). This critical point is associated with the point $(\frac{1}{2}\frac{1}{2}\frac{1}{2})$ where three frequency branches intersect, as required by symmetry. [See also A. E. Dixon, A. D. B. Woods, and B. N. Brockhouse, Proc. Phys. Soc. (London) **81**, 973 (1963).] Although none of the frequency gradients of these branches is zero at this point, nevertheless it gives rise to a "mild" critical point. This is presumably related to the fact that these three bands must all be distinct in the vicinity of this point. The same behavior occurs for potassium at $\nu=1.79\times10^{12}$ cps [see R. A. Cowley, A. D. B. Woods, and G. Dolling, Phys. Rev. **150**, 487 (1966)].

importance of obtaining the best possible force model which represents accurately the measured phonon dispersion curves.

Possible sources of error in this method have been discussed in GRI and we shall not repeat them unless additional considerations are involved. It is important to observe that most errors are eliminated by the enormous averaging out process, which is inherent in this method, but it is important to be aware of their existence. One source of error, which is important for the cubic case, is associated with twofold degeneracy for the transverse branch along the $\Lambda(qqq)$ direction (see GRI). This requires some caution in determining the Debye end of the spectrum. Such a degeneracy does not occur in the hcp crystal, because of different symmetry requirements, and hence one does not need a finer mesh at the origin Γ in order to increase the reliability of the calculation. There might, however, be another interesting source of error, which is not mentioned in GRI. This source of error is quite general and could be more important, the higher the order of the dynamical matrix (or, for that matter, if applied to electron density of states, the higher the order of the Hamiltonian matrix). This error originates from the fact that different bands belonging to the same irreducible representation cannot intersect.[14] It is apparent that for an arbitrary $\mathbf{q}_c$ (i.e., along some off-symmetry direction), the representation of the group of $\mathbf{q}_c$ cannot be reduced by symmetry operations, and hence, accidental degeneracies are not allowed for such a $\mathbf{q}_c$. This implies that in the vicinity of a $\mathbf{q}$ vector, where two or more bands are approaching each other, the respective gradients of these bands may undergo strong changes in order to avoid such an intersection. This might cast some doubt on the extent to which it is correct to approximate these gradients by constants inside volumes of finite sizes. We are convinced, however, that at least for the hcp lattices examined here, and even more so for monatomic cubic systems described in GRI that this error cannot be serious. A very efficient check on any source of statistical error is to compare $g(\nu)$ calculated for different numbers of mesh points. We have actually applied this test and found no significant changes[24] in $g(\nu)$ as a function of the number of mesh points provided this number is sufficiently large. The following argument also leads to the same conclusion. If the changes in the gradients are very abrupt as, for instance, in the vicinity of point H_1 and H_2 for Zn (Fig. 5), then its statistical effect on $g(\nu)$ would be very small. This is because abrupt changes in the gradient occur within a very small volume of the reciprocal lattice and thus cannot affect $g(\nu)$ appreciably. On the other hand, if these changes are moderate, their effect on the linear extrapolation assumption becomes less significant, but their influence occurs over larger volumes. This should make them more detectable when changing the mesh number, but, as stated previously, no significant effects were observed when the mesh number[24] was changed. In concluding this discussion on possible sources of errors, it is important to indicate that most of the considerations have been empirical and qualitative and that it is desirable to have a more quantitative analysis of this problem.

Before discussing the more physical conclusions that can be drawn from this article, it is worthwhile to emphasize a few points concerning the application of the method. It has been customary in the root-sampling method and also in the earlier version of the extrapolation method[2] to specify the number of frequencies used for the sampling. This is meaningless for the present method,[1] but rather an important indication should be the number of mesh points n used in the computation of $g(\nu)$. Naturally, $g(\nu)$ becomes smoother between critical points upon increasing this number n, but the size of n should be determined mainly by the purpose for which $g(\nu)$ is needed. For instance, for calculating thermodynamic properties, it is possible to use a considerably smaller n than would be necessary for very high resolution. On the other hand, it is advisable to use a larger n, even for the calculation of thermodynamic properties, if $g(\nu)$ is expected to have a complex structure. We found that the mesh numbers n quoted in this article were more than adequate for most purposes with the possible exception of those used for Mg. The channel width $d\nu$ is of much less critical importance. A too small $d\nu$ might prove to be a burden on the computer memory and it also increases computing time. On the other hand, a too large $d\nu$ obscures fine details, especially near critical points and close to $\nu=0$.

We hesitate to draw far-reaching conclusions on the basis of the models utilized throughout this article. These models describe in a more or less satisfactory manner the existing data, but disagreements could show up if experiments of coherent inelastic scattering of neutrons were extended to include more high-symmetry directions. Nevertheless, some general conclusions which are not particularly model-dependent can be drawn. It has been found that at least one strong critical point for each of the three lattices investigated originates from off-symmetry directions. The Θ^c of both Be and Zn should show a strong temperature dependence. Beryllium should be a suitable host for studying effects of heavy impurities, because of the large mass ratio of impurities over the host atoms, and also because there is a very large range of frequencies (about 50% of the entire range), for which $g(\nu)$ is very flat and of very low phonon density. Although Mg can also serve for such a purpose, because it shows no structure over about 50% of its frequency range, it is

[24] The changes that usually occurred as the mesh number was varied, were in small kinks which tended to change their location as a function of ν and also seemed to smooth out for an increasing mesh number n. This was also observed in the cubic lattices reported in GRI.

probably not as good because of its larger mass. The smaller mass ratio of impurity atoms to host atoms would tend to shift resonance modes toward the more populated region of $g(\nu)$.

In conclusion we want to indicate that this method could be extremely helpful for attempting accurate calculations of electron density of states. No such attempt has been made in the past, and to our best knowledge customary techniques of computations of electron density of states can be fairly crude and ambiguous. It is possible that this method would help to solve certain relevant problems.

ACKNOWLEDGMENTS

We wish to express our gratitude to Dr. H. C. Schweinler for many helpful discussions. One of us (L. J. R.) wishes to thank the Oak Ridge National Laboratory for the kind hospitality he enjoyed.

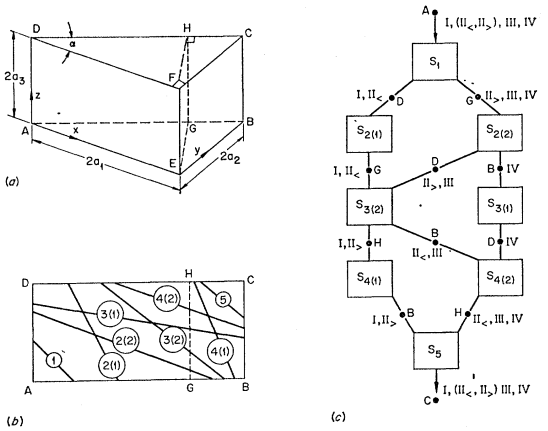

FIG. 9. (a) A right-angled triangular prism (wedge). (b) Two-dimensional projection of a wedge. The different cuts $j(m)$ are shown schematically. (c) Schematic summary of all possible cuts and sequences for a plane sweeping across the wedge. Use of the diagram is explained in this Appendix.

APPENDIX A

As explained in the text, we are interested in finding the cross-section area of the wedge (triangular prism) ABCDEF [Fig. 9(a)] as a function of the distance from a given point. Surface ABCD, being a mirror plane restricts the vector of the frequency gradient calculated at any point on this plane to lie in this plane. Another restriction imposed on the present calculation is that all angles at point E [Fig. 9(a)] are right angles. On the other hand, the angle α is not restricted. In Fig. 9(b) we view the wedge in two dimensions. HG is the perpendicular projection of the edge FE on ABCD. The lines 1, 2(1), 2(2), etc., represent the projections, on ABCD, of planes cutting the wedge. We next examine the behavior of the cross-section area of a plane, normal to the frequency gradient, which, starting from A, moves in the direction of its normal. In going from A to C the plane passes, in some order, through four intermediate corners (Fig. 9(b)]. This defines in total five different ranges through which w, the distance of the plane from A, varies. For any given w, we characterize a cut by $j(m)$, where j (equal to 1 through 5) is the number of corners on the left-hand side of the cut, according to Fig. 9(b). The same j also gives the range number. Whenever there are more than one possible cut for any given j, we label them with the index (m). Under the above conditions there are in total only eight distinct cuts. Obviously, before the first corner is reached, the cut is of type 1. Then, depending on whether this corner is D or G, the subsequent cut is either of type 2(1) or 2(2), and so forth. There are in total only five possible sequences in which the different cuts can follow each other. These sequences are labeled by Roman numerals I, II$_<$, II$_>$, III, and IV and are distinguishable by certain inequalities. The sequences together with these inequalities are listed in Table II. Sequences II$_<$ and II$_>$ are mutually exclusive, since II$_<$ requires $\alpha \leq 45°$, while for II$_>$, $\alpha \geq 45°$. The cross-section area for any cut $j(m)$ is $S_{j(m)}(w)$. In Fig. 9(c), we summarize the situation by a diagram. This figure correlates the sequences to the different ranges and cuts, and it also indicates the proper $S_{j(m)}(w)$ to be used in each case. Use of Fig. 9(c) as well as of Table II might best be illustrated by an

TABLE II. List of all possible sequences in which a plane can sweep across a triangular prism under the limitations described in the text. In the second column the geometrical conditions for each sequence are listed. In the rest of the columns the appropriate cross-section area $S_{j(m)}$ for each sequence and range are listed together with the respective range. t and c are tanα and cosα, respectively.

Sequence number	Conditions	Range number 1	2	3	4	5
I	$\lambda_3 \leq \min(\lambda_1, \lambda_1 t^2)$	S_1 $(0, w_{AD})$	$S_{2(1)}$ (w_{AD}, w_{AG})	$S_{3(2)}$ (w_{AG}, w_{AH})	$S_{4(1)}$ (w_{AH}, w_{AB})	S_5 (w_{AB}, w_{AC})
II$_<$ ($t^2 \leq 1$)[a]	$\lambda_1 t^2 \leq \lambda_3 \leq \lambda_1$	S_1 $(0, w_{AD})$	$S_{2(1)}$ (w_{AD}, w_{AG})	$S_{3(2)}$ (w_{AG}, w_{AB})	$S_{4(2)}$ (w_{AB}, w_{AH})	S_5 (w_{AH}, w_{AC})
II$_>$ ($t^2 \geq 1$)[a]	$\lambda_1 \leq \lambda_3 \leq \lambda_1 t^2$	S_1 $(0, w_{AG})$	$S_{2(2)}$ (w_{AG}, w_{AD})	$S_{3(2)}$ (w_{AD}, w_{AH})	$S_{4(1)}$ (w_{AH}, w_{AB})	S_5 (w_{AB}, w_{AC})
III	$\max(\lambda_1, \lambda_1 t^2) \leq \lambda_3 \leq \lambda_1 / c^2$	S_1 $(0, w_{AG})$	$S_{2(2)}$ (w_{AG}, w_{AD})	$S_{3(2)}$ (w_{AD}, w_{AB})	$S_{4(2)}$ (w_{AB}, w_{AH})	S_5 (w_{AH}, w_{AC})
IV	$\lambda_3 \geq \lambda_1 / c^2$	S_1 $(0, w_{AG})$	$S_{2(2)}$ (w_{AG}, w_{AB})	$S_{3(1)}$ (w_{AB}, w_{AD})	$S_{4(2)}$ (w_{AD}, w_{AH})	S_5 (w_{AH}, w_{AC})

[a] Sequences II$_<$ and II$_>$ are mutually exclusive for geometric reasons (see text).

TABLE III. List of all possible cross sections $S_{j(m)}$ together with the analytical expressions for $P_{j(m)}$, $Q_{j(m)}$, and $R_{j(m)}$. The following abbreviations are used in the table: $A=a_1a_2a_3/2\lambda_1\lambda_2\lambda_3$, $c^2\equiv\cos^2\alpha=\lambda_1/(\lambda_1+\lambda_2)$, $s^2\equiv\sin^2\alpha=\lambda_2/(\lambda_1+\lambda_2)$, $t^2\equiv\tan^2\alpha=\lambda_2/\lambda_1$.

$S_{j(m)}$	$P_{j(m)}$	$Q_{j(m)}$	$R_{j(m)}$
S_1	As^2	0	0
$S_{2(1)}$	0	$4A\lambda_3s^2$	$-4A\lambda_3^2s^2$
$S_{2(2)}$	$-Ac^2$	$4A\lambda_1$	$-4A\lambda_1^2$
$S_{3(1)}$	0	0	$4A\lambda_1^2t^2$
$S_{3(2)}$	$-A$	$4A(\lambda_1+\lambda_3s^2)$	$-4A(\lambda_1^2+\lambda_3^2s^2)$
$S_{4(1)}$	0	$-4A\lambda_3c^2$	$4A\lambda_3(2\lambda_1+\lambda_3c^2)$
$S_{4(2)}$	$-As^2$	$4A\lambda_3s^2$	$4At^2(\lambda_1^2-\lambda_3^2c^2)$
S_5	Ac^2	$-2A(\lambda_1+\lambda_3c^2)$	$(4A/c^2)(\lambda_1+\lambda_3c^2)^2$

example. Suppose λ_1 and λ_3, as defined by Eq. (3) in the text, satisfy the inequality conditions in Table II, so that a sequence is determined to be number III. Starting from A, the cut is of type 1 as long as we are in the first range, i.e., $w\leq w_{AG}$, and therefore the cross-section area is $S_1(w)$. After passing corner G the cut is in range 2(2) with cross-section area $S_{2(2)}$, which is true as long as $w_{AG}\leq w\leq w_{AD}$. Then, at the corner D, the cut goes over into type 3(2), implying the use of $S_{3(2)}$, and so forth.

The distances w_{AD}, w_{AG}, etc., which are used to determine the different ranges $j(m)$, are as follows:

$$\begin{aligned} w_{AD}&=2\lambda_3,\\ w_{AG}&=2\lambda_1,\\ w_{AH}&=2(\lambda_1+\lambda_3),\\ w_{AB}&=2\lambda_1/\cos^2\alpha, \end{aligned} \tag{A1}$$

and

$$w_{AC}=2\lambda_3+2\lambda_1/\cos^2\alpha.$$

The eight functions $S_{j(m)}(w)$ are at most second-order polynomials in w, and hence can all be written as

$$S_{j(m)}(w)=P_{j(m)}w^2+Q_{j(m)}w+R_{j(m)}. \tag{A2}$$

The coefficients $P_{j(m)}$, $Q_{j(m)}$, and $R_{j(m)}$ depend on λ_i and are tabulated in Table III. Use is made of the restriction that the normal to all cuts must lie in the mirror plane $ABCD$; this yields the condition

$$\lambda_2/\lambda_1=\tan^2\alpha. \tag{A3}$$

The property mentioned in the text about the smooth behavior of $S(w)$ and dS/dw, as a corner is passed, facilitates the task of calculating the various expressions for $S_{j(m)}(w)$. The volume between any two parallel planes at distances w_1 and w_2, respectively, is simply the integral of the appropriate $S_{j(m)}(w)$ between these limits. The partial distribution $g(j,\mathbf{q}_c,\nu)$ can now be calculated with Eq. (2) in the text, where $W_{\mathbf{q}_c}$ is unity and w_4, in the expression for the range of variation of ν, has to be replaced by $W_{Ac}/2$ because of the different geometric situation.

An equivalent choice of origin could be C rather than A, which amounts to choosing new axes x', y', and z', corresponding to $(2a_2-y)$, $(2a_1-x)$ and $(2a_3-z)$, respectively. The cross-section area $S_{j(m)}$ in the old system is identical to $S_{6-j(m)}$ in the new frame and satisfies:

$$\begin{aligned} S_{6-j(m)}(\lambda_2,\lambda_1,\lambda_3;\{2(\lambda_1+\lambda_2+\lambda_3)-w\})\\ =S_{j(m)}(\lambda_1,\lambda_2,\lambda_3;w). \end{aligned} \tag{A4}$$

APPENDIX B

We give the relations between the MAS model and the four-neighbor tensor force model (TF). We adopt the notation of DeWames *et al.*[5] for the MAS model, and of Iyengar *et al.*[10,13] for the TF model so that the parameters appropriate to the MAS model are on the left-hand side of the equations. The abbreviation γ_0 is

TABLE IV. List of the allowable irreducible representations for all the high-symmetry directions and points of hcp lattices (see Fig. 1). In the third column are listed the point group associated with each point or direction. The last column lists the degenerate representations.

Point or direction	Allowable irreducible representation	Little group	Degeneracies
Γ	$\Gamma_2^-+\Gamma_3^++\Gamma_5^++\Gamma_6^-$	D_{3h}	Γ_5^+ and Γ_6^- (twofold)[a]
A	A_1+A_3	D_{6h}	A_1 (2-fold), A_3 (fourfold)
K	$K_1+K_2+K_5+K_6$	D_{3h}	K_5 and K_6 (twofold)
H	$H_1+H_2+H_3$	D_{3h}	H_1, H_2 and H_3 (twofold)
M	$M_1^++M_3^++M_4^++M_2^-+M_3^-+M_4^-$	D_{2h}	
L	$2L_1+L_2$	D_{2h}	L_1 and L_2 (twofold)
Δ	$\Delta_1+\Delta_2+\Delta_5+\Delta_6$	C_{6v}	Δ_5 and Δ_6 (twofold)
Σ	$2\Sigma_1+2\Sigma_3+2\Sigma_4$	C_{2v}	
T	$2T_1+T_2+T_3+2T_4$	C_{2v}	
T'	$2T_1'+T_2'+T_3'+2T_4'$	C_{2v}	
R	$2R_1$	C_{2v}	R_1 (twofold)
S	$2S_1$	C_{2v}	S_1 (twofold)
S'	$2S_1'$	C_{2v}	S_1' (twofold)
P	$2P_1+2P_3$	C_{3v}	P_3 (twofold)
U	$2U_1+U_2+2U_3+U_4$	C_{2v}	

[a] Additional degeneracy between Γ_2^- and Γ_5^+ is required by time reversal.

used for the c/a ratio (not to be confused with the force constant γ).

$$\delta_1=-\mu,$$
$$\epsilon_{1x}=\lambda+2\mu,$$
$$\epsilon_{1z}=3\gamma_0^2\mu+\nu,$$
$$\alpha_2=4\beta,$$
$$\beta_{2x}=\alpha-2\beta,$$
$$\beta_{2z}=\gamma,$$
$$\delta_3=-\tfrac{1}{4}\eta,$$
$$\epsilon_{3x}=\zeta+2\eta,$$
$$\epsilon_{3z}=\tfrac{3}{4}\gamma_0^2\eta+\zeta,$$
$$\alpha_4+\beta_{4z}=\phi,$$
$$\beta_{4x}=\theta.$$

APPENDIX C

In this section we describe briefly the classification of the normal modes by the irreducible representations of the space groups for the high-symmetry directions and points (Fig. 1). The irreducible representations of the point groups were obtained by Koster.[4] Iyengar *et al.*[10] worked out the character tables for some of the points and directions (namely, Γ, A, K, M, Δ, Σ, and T in Fig. 1). We summarize the classification of the modes by irreducible representations in Table IV. In addition we give a few compatibility relations which facilitate the correct identification of points with branches.

For point M and directions Σ, T', and U, these relations are

$$\Sigma_1\rightarrow M_1^+ + M_2^-,$$
$$\Sigma_3\rightarrow M_3^+ + M_4^-,$$
$$\Sigma_4\rightarrow M_4^+ + M_3^-,$$
$$T_1'\rightarrow M_1^+ + M_3^-,$$
$$T_2'\rightarrow M_3^+,$$
$$T_3'\rightarrow M_4^-,$$
$$T_4'\rightarrow M_2^- + M_4^+,$$
$$U_1\rightarrow M_1^+ + M_4^-,$$
$$U_2\rightarrow M_3^-,$$
$$U_3\rightarrow M_3^+ + M_2^-,$$
$$U_4\rightarrow M_4^+;$$

for point K and directions T, T', and P, these relations are

$$T_1,T_1'\rightarrow K_1+K_5,$$
$$T_2,T_2'\rightarrow K_6,$$
$$T_3,T_3'\rightarrow K_6,$$
$$T_4,T_4'\rightarrow K_2+K_5,$$
$$P_3\rightarrow K_5+K_6,$$
$$P_1\rightarrow K_1+K_2;$$

for point L and direction U

$$L_1\rightarrow U_1+U_3,$$
$$L_2\rightarrow U_2+U_4;$$

and finally for point H and direction P

$$P_1\rightarrow H_1,$$
$$P_3\rightarrow H_2+H_3.$$

APPENDIX D

Here we describe the way in which a typical mesh has been constructed to perform the computation of $g(\nu)$ described in this article. Let N_x and N_z be the number of mesh points along the x and z axes, respectively. The integers n_x, n_y, and n_z satisfy $n_y\leq n_x\leq N_x$ and $n_z\leq N_z$. If we restrict ourselves to the irreducible zone shown in Fig. 1 of the text, then a general mesh point $\mathbf{q}_c$ inside this zone, or possibly on the surface ΓKHA, will have the following components:

$$\begin{aligned} q_{cx}&=(2\pi/\sqrt{3}aN_x)(n_x-\tfrac{1}{2}),\\ q_{cy}&=(2\pi/3aN_x)(n_y-\tfrac{1}{2}), \qquad n_y\leq n_x\leq N_x\\ q_{cz}&=(\pi/cN_z)(n_z-\tfrac{1}{2}). \qquad n_z\leq N_z \end{aligned} \tag{D1}$$

This choice ensures that all mesh points are inside the irreducible zone except for some points on the plane ΓKHA. Although no restriction is required for the ratio N_x/N_z, it has been chosen to be as close as possible to $(2c/\sqrt{3}a)$. The number n of mesh points chosen in this manner is given by

$$n=\tfrac{1}{2}N_zN_x(N_x+1). \tag{D2}$$